Transmission electron microscopy investigation of interfacial reactions between SrFeO3 thin films and silicon substrates

Wang, Dashan; Tunney, Jim; Du, Xiaomei; Post, Michael; Gauvin, Raynald

Publisher's version / Version de l'éditeur:
https://doi.org/10.1557/JMR.2007.0005
Journal of Materials Research, 22, 1, pp. 76-88, 2007

Transmission electron microscopy investigation of interfacial reactions between $SrFeO_3$ thin films and silicon substrates

Dashan Wang[a], James J. Tunney, Xiaomei Du, and Michael L. Post
Institute for Chemical Process and Environmental Technology, National Research Council of Canada, Ottawa, Ontario, Canada K1A 0R6

Raynald Gauvin
Department of Mining, Metals and Materials Engineering, McGill University, Montreal, Quebec, Canada H3A 2B2

(Received 11 July 2006; accepted 24 August 2006)

The $SrFeO_3/SiO_2/Si$ thin film system has been studied using transmission electron microscopy (TEM). The thin films of $SrFeO_3$ were grown by pulsed laser deposition onto silicon substrates with a SiO_2 buffer layer at room temperature (RT) and 700 °C and subjected to annealing for various periods of time at temperature $T = 700$ °C. Transmission electron microscopy characterization showed that the microstructure of the film deposited at room temperature contained crystalline and amorphous layers. Silicon diffusion into $SrFeO_3$ films occurred at the SiO_2 interface for the samples deposited at 700 °C and for those films annealed at 700 °C. The silicon diffusion-induced interfacial reactions resulted in the phase transformations and the growth of complex crystalline and amorphous phases. The principal compositions of these phases were $Sr(Fe,Si)_{12}O_{19}$, SrO_x and amorphous [Sr-Fe-O-Si].

I. INTRODUCTION

Perovskite and its related oxides have attracted considerable interest due to its extensive applications in a number of technological areas such as materials for catalysis[1] and solid state gas sensors.[1–8] Perovskites based on the non-stoichiometric family $SrFeO_{2.5+x}$ ($0 < x < 0.5$) display different crystal structures depending on the degree of oxygen stoichiometry.[9–12] The end member phases for these compounds are the orthorhombic brownmillerite form at $x \sim 0$ and cubic or pseudo-cubic perovskite at $x > 0.4$. At intermediate oxygen stoichiometry, phases based on a distorted cubic structure exist; these are tetragonal and orthorhombic structures that possess longer range ordering of the oxygen sub-lattice. $SrFeO_{2.5+x}$ materials can be used as thin film gas sensors[6,7,11,12] because the reversible uptake of oxygen at elevated temperatures can readily occur, and this is accompanied by significant changes in electrical conductivity that can be monitored as the sensor transduction signal.

The electrical and gas sensing properties of films of these material types are strongly dependent on the cation and oxygen stoichiometries[7] and also on film morphology.[13–16] However, both the structure and the morphology of the films are dependent on deposition temperature, and studies have shown that films deposited at different temperatures have varying degrees of crystallinity and preferential orientation.[17,18] Films that exhibit no crystallinity or texture show limited sensor functionality and cannot easily and reversibly transform from the brownmillerite to the cubic perovskite structures. Thus, a full understanding of the effects of deposition conditions, especially the roles of deposition temperature and post-deposition thermal treatments, on the film structure is crucial for optimizing the gas sensor response characteristics.

In addition to the sensitivity and rapid response of the sensors, thermal stability of the thin film must also be considered to ensure longer term signal reproducibility because perovskite based gas sensors are operated at elevated temperature to provide a rapid sensor response. The perovskite materials may be unstable under certain thermochemical conditions,[19] and at the elevated operating temperatures of ceramic-based gas sensors the films may react with the underlying substrate.[20–26] This is especially important for microelectromechanical system (MEMS)-based sensors using silicon-based sensor platform structures[27] because silicon is known to react with many materials at elevated temperatures ($T > 300$ °C).[22–26,28,29] Therefore, a comprehensive understanding of the inter-relationships between the thin film sensor material and the underlying substrate is

[a]Address all correspondence to this author.
e-mail: dashan.wang@nrc.ca
DOI: 10.1557/JMR.2007.0005

crucial in determining sensor stability and design, especially for devices that will be operated at elevated temperatures (>300 °C).

In the present article, thin films of $SrFeO_{2.5+x}$ where $x > 0.4$ (hereafter designated as $SrFeO_3$) have been grown onto single crystal silicon substrates by the pulsed laser deposition (PLD) technique. The films have been prepared under different growth conditions and subjected to post-deposition thermal treatments. The structure of the films and interface regions was comprehensively investigated using analytical transmission electron microscopy including high resolution imaging, electron diffraction, and energy dispersive spectrometry.

II. EXPERIMENTAL PROCEDURE

Powdered $SrFeO_3$ was synthesized by conventional ceramic preparation techniques. Stoichiometric amounts of $SrCO_3$ and Fe_2O_3 precursor powders (Alfa-Aesar, Ward Hill, MA, >99.99% purity on a metal basis) were mixed and ground, and then heat treated at 1100 °C under oxygen in a tube furnace for 36 h. The sintered product was then ground and characterized by x-ray diffraction (XRD) (Bruker Axis D8 diffractometer, monochromatic Cu-K_α radiation, scan range $5° \leqslant 2\theta \leqslant 100°$; step size 0.03°; dwell time 2 s) to ensure that a single-phase product was obtained. The $SrFeO_3$ powder (2 g) was then pelletized in a mold in a hydraulic press at 2T and resintered at 1150 °C in oxygen to yield a dense cylindrical pellet with dimension 12 mm(dia) × 5 mm. Further XRD analysis confirmed the pellet to be single phase.

The $SrFeO_3$ pellet was then used as the target material for the deposition of $SrFeO_3$ thin films by the pulsed laser deposition (PLD) technique. The excimer laser used was a Lambda Physik LPX305i (Goettingen, Germany), operating with Kr/F ($\lambda = 248$ nm); other system details are reported elsewhere.[11] The substrates for the films were cut sections (1 cm × 1 cm) of a single crystal silicon(111) wafer that had a preformed, thermally grown layer of silica (SiO_2) of 2 μm thickness. During deposition, the temperature of the substrate was maintained at either room temperature (RT ~ 22 °C) or 700 °C. All films were deposited for 4 min at a laser pulse rate of 8 Hz, pulse duration of 25 ns, fluence of ~1.5 $J.cm^{-2}$ and under a background oxygen pressure of 100 mTorr. The average deposition rate was about 10–20 nm per minute depending on deposition temperature, producing films of approximately 40–80 nm thickness.

Cross-section and plan view specimens of the $SrFeO_3$ films on the Si/SiO_2 substrates were then prepared for TEM examination.[30,31] For cross-section specimen preparation, two pieces approximately 5 mm long and 1 mm wide were cleaved from the deposited thin film wafer and glued together with epoxy adhesive, film side face to face to form a sandwich or a raft-like structure along with pieces of the same size cleaved from a bare silicon wafer that was just over 3 mm thick. The epoxy was then cured at $T \sim 100$ °C in air, and the raft was cut to form a disc 3 mm in diameter with a Gatan Ultrasonic Disc Cutter (Model 601). The disc was mechanically ground using a Gatan specimen grinder with abrasive paper (finished at 600 grit) to a thickness of less than 100 μm. The upper and lower surfaces were then dimpled using an EAF Specimen Prep System, Model 2000 and polished with 0.25 μm diamond paste at the final stage to produce a mirror finish and a small hole less than 0.3 mm in the center. The edges of the specimen adjacent to the hole were Ar-ion milled using a Gatan Precision Ion Polishing System (PIPS), Model 691 for about 40 min at 4 kv and an incident angle of ~10° to the surface followed by ~20 min at 2–3 kV. This provided imaging access to the subject film and associated interfaces with the substrate.

For the preparation of a plan view specimen, a 3 mm disc was cut from the deposited thin film wafer. This piece was ground from the underside to approximately 100 micrometer thickness, followed by dimpling to provide a region with a thickness of about 10 μm. Final thinning to perforation was achieved by single-sided sputtering. Specific layers of the multilayered films were accessed by incremental steps of Ar-ion sputtering to remove the upper layers using a Gatan PIPS system.

Characterization and imaging by TEM was done using a Philips CM20 TEM system equipped with an energy dispersive x-ray spectrometer: INCA Energy TEM 200 and a Gatan UltraScan 1000 CCD camera. An accelerating voltage 200 kV was selected for TEM imaging and a beam size smaller than 10 nm was used for energy dispersive spectroscopy (EDS) chemical composition analysis. Bright field (BF), dark field (DF), high resolution (HR) TEM imaging, and electron diffraction (ED) techniques were used to investigate the crystallographic and interfacial structure of the films.

III. RESULTS AND DISCUSSION

A. Structures of $SrFeO_3/SiO_2/Si$ thin films deposited at room temperature

The BF TEM images obtained from a cross-section specimen of the $SrFeO_3/SiO_2/Si$ thin film system deposited at ambient temperature are shown in Fig. 1. The $SrFeO_3$ film was measured to be 46 nm in thickness and the adjacent buffer layer of SiO_2 was 1.14 μm in thickness [Fig. 1(a)]. High resolution TEM (HRTEM) images [Fig. 1(b)] show that the $SrFeO_3$ film is constituted by two regions. One is a layer of nano-sized grains, about 5 nm in diameter, with fringe features having crystalline characteristics. The other, beneath the nanograins, is a layer of featureless domains interfacing with the amorphous SiO_2 buffer layer. An amorphous/single crystal

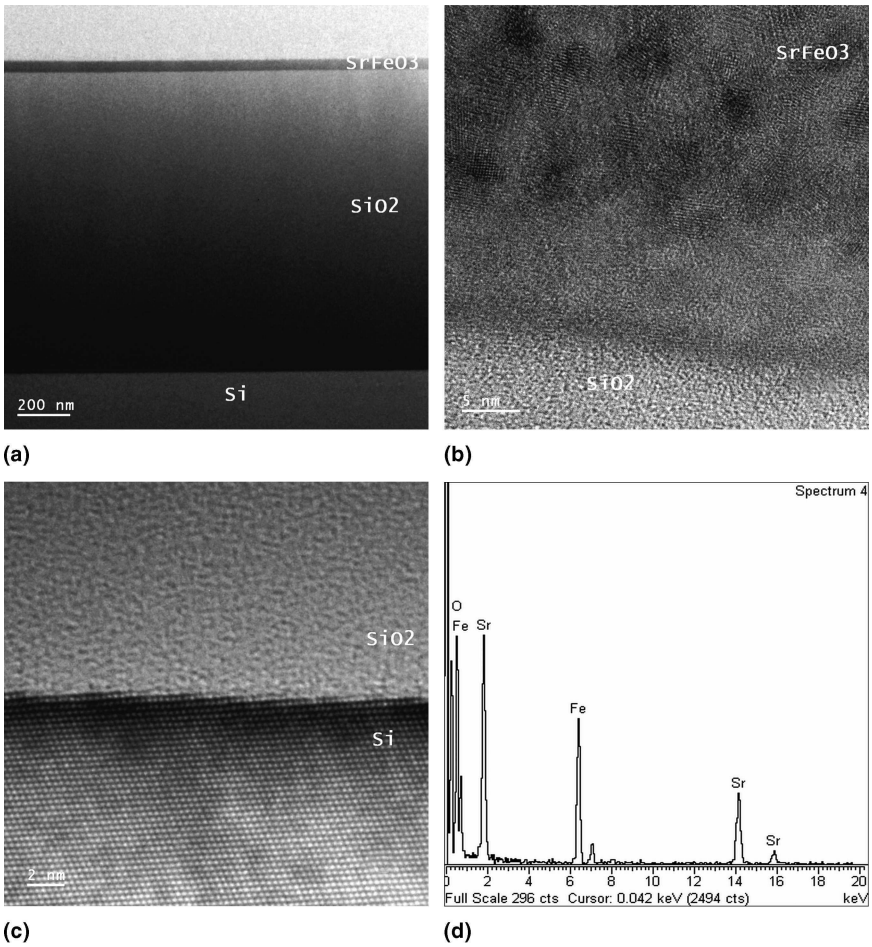

FIG. 1. TEM micrographs (a–c) from a cross-section specimen of the $SrFeO_3$ thin film deposited onto the SiO_2/Si substrate at room temperature for 4 min. (a) A complete view of the cross section of the thin films system. (b) HRTEM image of the thin film of $SrFeO_3$ and its adjacent SiO_2 layer. The $SrFeO_3$ thin film consists of a layer of crystalline nanosized $SrFeO_3$ grains and a layer of featureless domains adjacent to the amorphous SiO_2 layer. (c) HRTEM image showing the interface of SiO_2/Si. (d) EDS spectra showing the chemical composition of the $SrFeO_3$ layer.

structure characterizing the interface between the silica layer (SiO_2) and the silicon (111) substrate is shown in Fig. 1(c). Energy dispersive x-ray analysis (EDS) [Fig. 1(d)] confirms that the $SrFeO_3$ film had elemental composition corresponding to that of the target used in the PLD step. No chemical inter-diffusion of elements was found across the $SrFeO_3/SiO_2$ interface.

For the $SrFeO_3$ film, which is adjacent to the SiO_2 layer, there exists a 15 nm layer that shows featureless domains, and is likely to be amorphous [Fig. 1(b)]. This implies that the amorphous SiO_2 layer provided a surface unfavorable to the required conditions to induce nucleation. Consequently, an amorphous $SrFeO_3$ region initially forms on the SiO_2 as a transition zone before the nucleation of crystalline $SrFeO_3$.

B. Structures of $SrFeO_3/SiO_2$/Si thin films deposited at 700 °C and post-deposition thermal treatment

An as-deposited thin film of $SrFeO_3/SiO_2$/Si grown at 700 °C for 4 min was investigated, and shown in Fig. 2 is a BF TEM cross-section micrograph of this system. The image [Figs. 2(a) and 2(b)] shows a face-to-face contact of the film with a light colored layer (sample preparation adhesive) in between. The total thickness of the $SrFeO_3$ film is 70 nm with principal features in the $SrFeO_3$ film that distinguish two types of layer on the SiO_2 buffer layer of the substrate: an upper region of about 15 nm and a lower layer of about 55 nm adjacent to the SiO_2.

Overall, the $SrFeO_3$ film is much thicker compared with the $SrFeO_3/SiO_2$/Si system deposited at room temperature because of the significant growth of the amorphous layer in the film deposited at 700 °C as shown in Fig. 2(b). The upper layer of the film contains a continuous layer of crystalline grains, denoted as Sr-Fe-O, embedded in the lower layer, which is amorphous, denoted as Sr-Fe-O-Si. The upper grains are aligned to form a monolayer about 15 nm thick. The two-layer structure in the film is similar to that of the film deposited at room temperature but with different relative thicknesses. This is likely due to the higher deposition temperature and

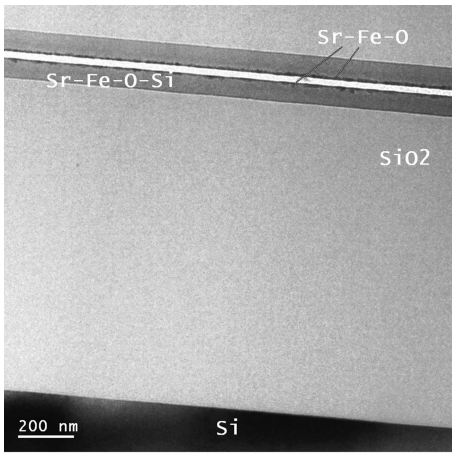

(a)

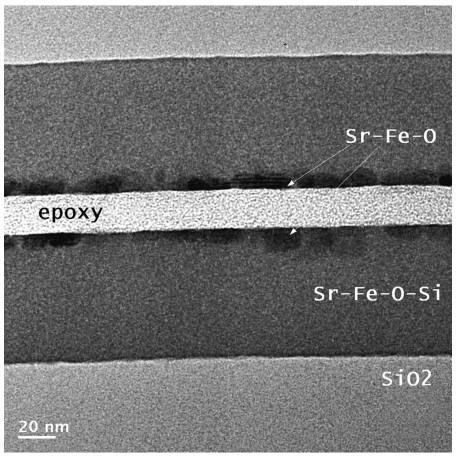

(b)

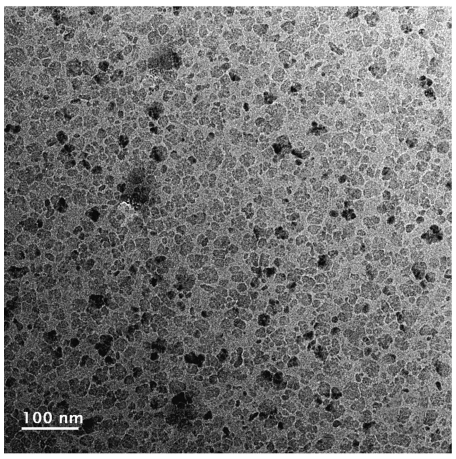

(c)

FIG. 2. BF TEM micrographs taken from a cross-section specimen of the thin film system $SrFeO_3$ /SiO_2/Si deposited at 700 °C for 4 min. (a) The film/substrate structure containing top grains labeled as Sr-Fe-O and a layer of amorphous phase labeled as Sr-Fe-O-Si. (b) A cross-section image of the film system with higher magnification showing a continuous layer of grains on the surface of the film. Note: images are obtained from a cross-section specimen showing two sample pieces that were face-to-face glued together with epoxy. (c) A plan view image of the film where grains are viewed to be uniform in size and the grain size is measured to be 15 nm in average.

consequently higher diffusion rates occurring at the SiO_2 interface, which favors the growth of the amorphous phase. Compared to the case of room temperature deposition, there is a thickening of the amorphous phase and a thinning of the crystalline layer of the grains in the high temperature deposited film. This provides evidence that deposition at the higher temperature resulted in increased growth of the amorphous phase by reaction with the SiO_2 layer and with the crystalline grains in the film. In addition, the cross-section and plan view images of the crystalline grains presented in Figs. 2(b) and 2(c) show that they are predominantly around 15 nm in dimension. The SiO_2/Si interface structure remained the same as in the case of the film deposited at room temperature.

Energy dispersive spectroscopy analysis of the film on a cross-section sample showed that the elemental compositions were different from those found in the films deposited at room temperature, and where the composition in the deposited film (in the nanocrystalline and amorphous regions) is identical to $SrFeO_3$. A slightly larger relative amount of iron is present in the crystalline grains shown in Fig. 3(a), as compared with the spectra of the crystalline $SrFeO_3$ phase shown in Fig. 1(d). The slight variation from the stoichiometry of $SrFeO_3$ implies that a structural defect or even phase transformation could occur. Significant differences between the crystalline and the amorphous phases in the film deposited at 700 °C can be seen from the spectra shown in Figs. 3(a) and 3(b) (i.e., in the amorphous phase of the film, a smaller relative amount of iron and significant amount of Si are present, unlike the case of room temperature deposited film where the composition in the nanocrystalline and amorphous region are identical). Note that because the Si (K_α) peak (at 1.739 keV) and the Sr(L_α) peak (at 1.806 keV) overlap in the EDS spectra, the existence of silicon in the crystallites cannot be confirmed by distinguishing these two peaks in the EDS spectra, particularly when the relative amount of silicon is small. However, by comparing these spectra with those for $SrFeO_3$, the existence of Si can be confirmed by calculating the ratio of the peak height of Sr(L) to Sr(K) or Sr(L) to Fe(K) in each spectrum respectively and taking the one of $SrFeO_3$ as a standard for calibration. As a result, the amorphous part of the film is determined to contain additional silicon [Fig. 3(b)]. EDS also confirmed that in the SiO_2 region close to the $SrFeO_3$/SiO_2 interface, there was no Fe or Sr present [Fig. 3(c)]. Thus, a reaction can be inferred as a Si diffusion through the $SrFeO_3$/SiO_2 interface resulting in the formation and growth of the layer-like amorphous Sr-Fe-O-Si phase.

Crystallographic characteristics of the film were also determined. Shown in Fig. 4(a) is a cross-section image of an individual grain that shows a single crystallite attached to two or three smaller grains as indicated by an arrow. Since the outermost part of the film represented

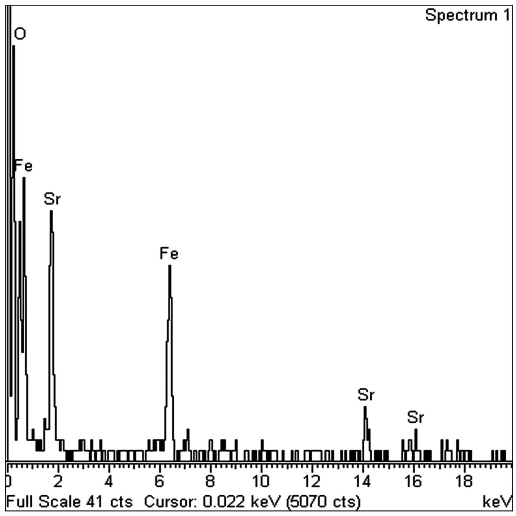

(a)

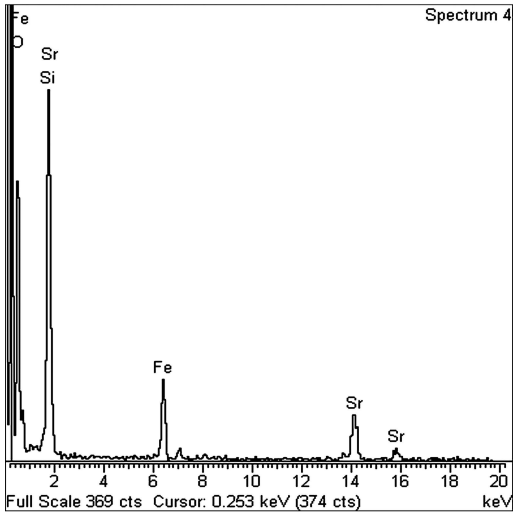

(b)

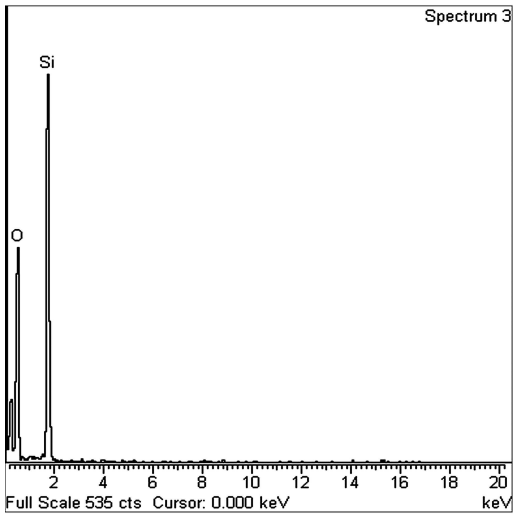

(c)

FIG. 3. EDS spectra of the thin film system $SrFeO_3/SiO_2/Si$ deposited at 700 °C for 4 min (a) from the crystal grains in the film, (b) from the amorphous phase of the film, and (c) from the SiO_2.

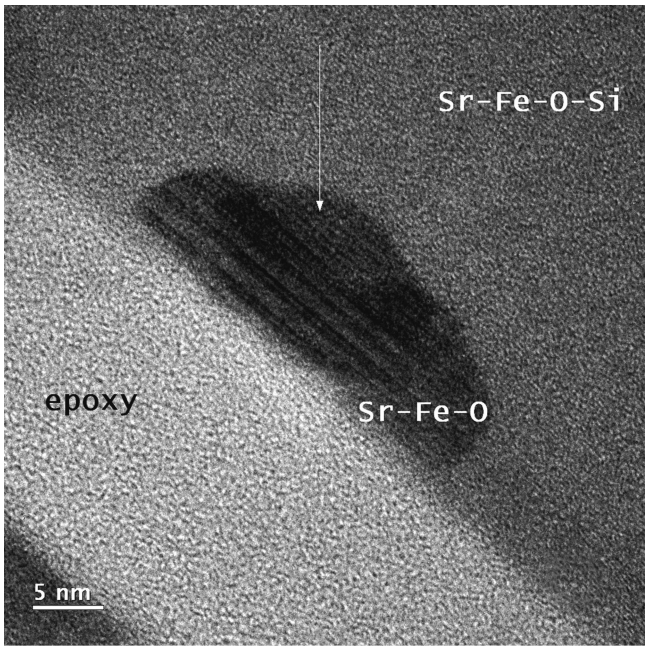

(a)

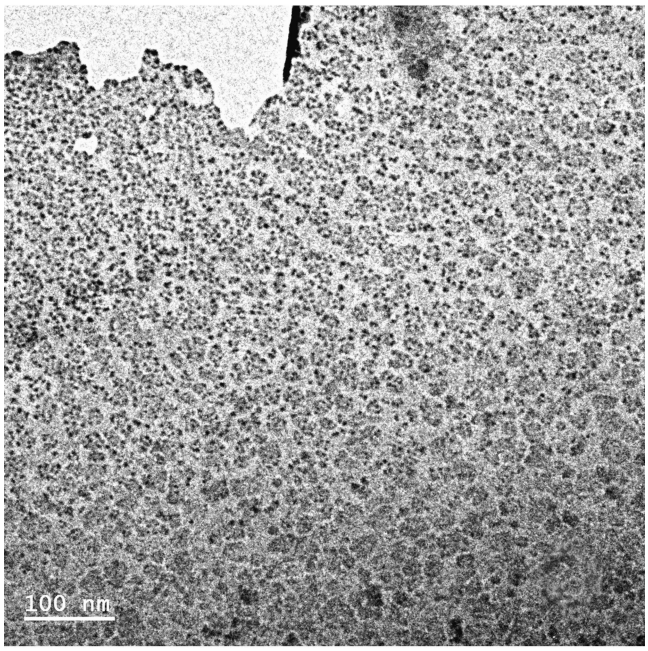

(b)

FIG. 4. (a) A cross-section image of an individual grain from the $SrFeO_3/SiO_2/Si$ thin film system deposited at 700 °C for 4 min showing that a single crystallite is attached by two or three small grains. (b) A TEM plan view image of the film showing the crystalline grains, where the top layer crystallites (near the top left area) are removed.

by the larger crystallite appears to be preferentially orientated and boundaries occur between the larger crystallite and the attached smaller grains, the possibility of multi-phase was taken into account in phase identification. To identify these crystalline phases, a plan view specimen was prepared to remove the outermost

crystallites by argon ion sputtering, leaving the small grains underneath remaining as shown in the upper left area of Fig. 4(b). A selected area (SA) electron diffraction pattern (EDP) [Fig. 5(a)] was then obtained from this area. The EDP shown in Fig. 5(b) was obtained from the outermost larger grains of the non-surface sputtered film as shown in Fig. 2(c). For comparison, an EDP of polycrystalline $SrFeO_3$ is also presented in Fig. 5(c). It is apparent that the EDPs shown in Figs. 5(a) and 5(b) represent crystal structures different from that of $SrFeO_3$. Considering that the slight difference in chemical composition between the grains in the as-deposited film and the crystalline $SrFeO_3$, as shown in Figs. 3(a) and 1(d), is not a strong cause to give a critical impact on the crystal structure of the film, and the compound $SrFeO_3$ is thermal stable under the deposition temperature, it is reasonable to assume that the crystal structure of these crystalline grains still remains the same as that for $SrFeO_3$. The slight difference in composition could only introduce crystal defects to the $SrFeO_3$ structure. The differences in the EDPs imply that the crystallites possess preferential orientations.

The pattern shown in Fig. 5(a) consists of a set of diffraction rings including the low angle diffuse ring close to the center BF spot. The diffuse ring occurring with ring patterns indicates that a mixture of amorphous and crystalline phases exists. The amorphous phase, in this case, is likely the Sr-Fe-O–Si compound with short-range ordered domains [Fig. 5(d)]. A sharper diffraction ring overlaps the diffuse ring shown in Fig. 5(a) suggesting that reflections from crystals represent those crystalline planes with a *d*-spacing identical to the average atomic spacing of the short-range ordered domains in the amorphous phase. The co-existence of crystalline and amorphous phases is the result of the tolerance in nucleation of the film and the growth of the amorphous phase underneath.

The interface between the crystallites and the amorphous phase becomes the growth front of the amorphous phase as it consumes the crystallites in the film.

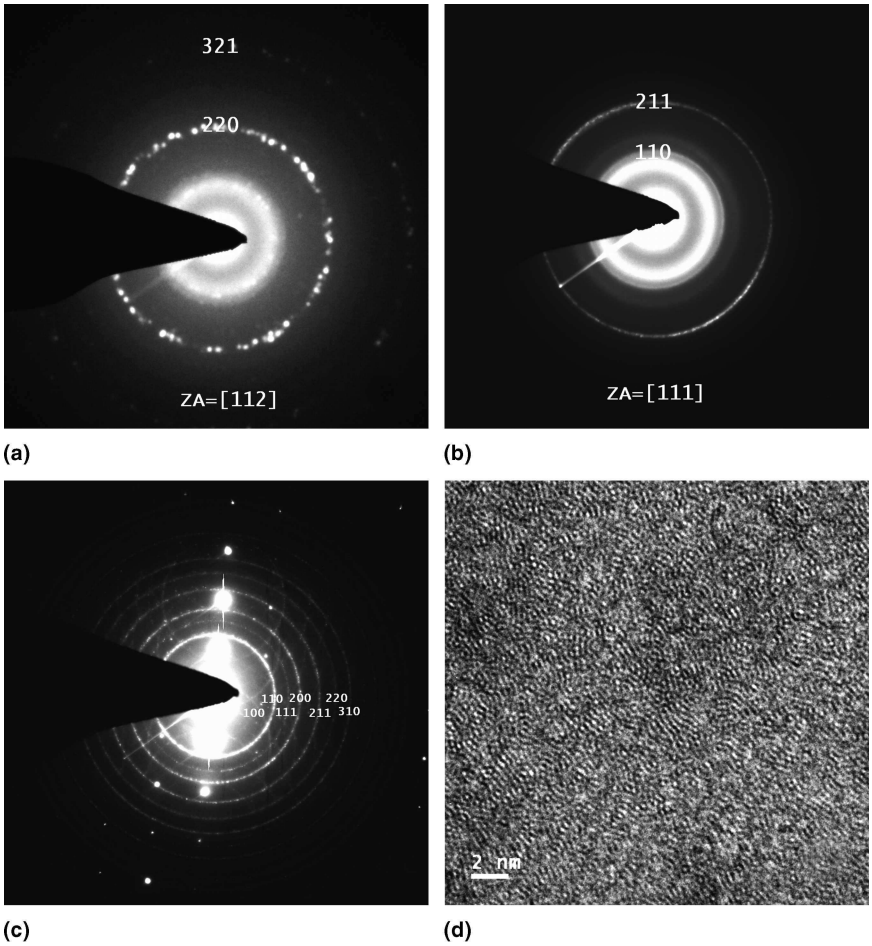

FIG. 5. For the $SrFeO_3/SiO_2/Si$ thin film system deposited at 700 °C for 4 min, (a) an SAD pattern from the top left area near the edge shown in Fig. 4(b) indexed as ZA = [112]. (b) An SAD pattern from the outermost larger grains of the non-surface sputtered film as shown in Fig. 2(c) indexed as ZA = [111]. (c) An ED pattern from $SrFeO_3$. (d) An image of the amorphous phase Sr-Fe-O-Si with atomic short-range ordered domains.

Therefore, the small grains attached to the outmost crystallites can be considered to be either the primary nuclei on the amorphous phase or the remnants of the crystalline phase following amorphous growth. Nevertheless, the small grains provide a site for the outermost crystallites to grow with a new preferred orientation.

Assuming that the crystalline grains possess the pseudo cubic structure of $SrFeO_3$, then those crystallites adjacent to the amorphous phase (Sr-Fe-O-Si) have a preferential orientation of [112] perpendicular to the film surface as indicated in Fig. 5(a). The diffraction pattern from crystallites at the top surface of the film gives *d*-spacings closest matching the (110) and (211) planes of the phase $SrFeO_3$ ($d_{110} = 0.2635$ nm, $d_{211} = 0.1516$ nm, less than 4% difference from d_{110} and d_{211} of $SrFeO_3$ indicated in PDF No. 34-0641). As a result, a preferential orientation of [111] is determined to be present in the outermost grains because only the diffraction pattern with ZA = [111] allows both the (110) and (211) reflections to occur simultaneously. Although the two sets of SA EDPs share some similarities, differences are present between the patterns as shown in Figs. 5(a) and 5(b). For example, the *d*-spacings calculated for the diffraction rings with similar intensities in the two sets of patterns; i.e., the diffraction rings indexed as (220) in Fig. 5(a) and (211) in Fig. 5(b) are not identical ($(d_{220})_{ZA=[112]} = 0.9\ (d_{211})_{ZA=[111]}$). Hence, different preferential orientations were considered to be present for the grains as discussed previously, and they are indexed as ZA = [112] and ZA = [111] for crystallites adjacent to the amorphous phase (Sr-Fe-O-Si) and outermost crystal grains, respectively.

It should be noted that because the film was deposited on a single crystalline Si (111) wafer with a SiO_2 buffer layer, the preferential orientation of the crystalline grains are determined by initially obtaining an electron diffraction pattern from the substrate Si area with zone axis ZA = [111], which is perpendicular to the surface. The electron diffraction image was then taken from the region of interest by translating the specimen using the TEM specimen holder. Considering that an amorphous buffer layer of SiO_2 exists between the deposited film and the single crystal Si substrate, this acted as a barrier and prevented the nucleation and growth of the crystalline grains of the deposited film from the influence of the crystalline Si substrate. Therefore, it is more meaningful to take the orientation of the surface rather than that of the Si as the reference for defining the preferential orientation of the crystal grains in the film. However, the orientation of the area chosen for electron diffraction could be tilted from the perpendicular to the Si [111] direction, and this is attributed to the localized tilt of the film due to a combination of film deformation and the setting precision of the specimen holder.

To investigate whether phase transformation or phase separation could occur in the films during heating at elevated temperature, TEM examination was performed on the thin film system $SrFeO_3/SiO_2/Si$ grown at 700 °C with a further 1 h of thermal annealing at $T = 700$ °C in air following the deposition. TEM images and EDS spectra for this film are shown in Fig. 6. Annealing produces some significant structural modifications compared to as-deposited films. The thickness of the $SrFeO_3$ film was reduced to 52 nm, which includes about 10 nm of a crystalline phase (grains) on the top surface and 42 nm of an amorphous phase underneath [Figs. 6(a) and 6(b)]. One of the possible causes of reduced film thickness is an increase in film density during crystal growth. Also, a continuous crystalline layer of Sr-Fe-O in the film is observed in Fig. 6(b), consisting of disk-like grains with lattice-scaled lamellar features parallel to the surface [see HRTEM image in Fig. 6(c)]. The crystallites are well formed unlike the grains shown in Fig. 4(a), and are embedded in the amorphous Sr-Fe-O-Si phase. The interface between the film and the SiO_2 of the substrate is no longer as flat as it was before annealing, implying that an interfacial reaction occurred during deposition and/or annealing.

Analysis by EDS showed the elements in each phase to be the same as those present in the sample prior to annealing. However, the relative amount of (Sr, Fe, and O) in the crystalline layer is significantly different [Fig. 6(d)] with the relative amount of Fe increased. Also, for the amorphous phase, either the relative amount of Fe is reduced, or the amount of strontium is increased [Fig. 6(e)]. This is in addition to the existence of a significant amount of Si, which has been shown to be present in the amorphous phase in the sample before annealing. By analyzing the spectra shown in Fig. 6(d) and comparing with the spectra for $SrFeO_3$, it is reasonable to assume that silicon is present in the crystallites of the outermost layer and it is a phase with composition richer in Fe relative to Sr.

Shown in Fig. 7(a) is an EDP obtained from the crystallites present in the outermost layer of the film after annealing at 700 °C for 1 h. This diffraction pattern differs from any obtained with the previously discussed samples. Combining the information of the electron diffraction and the EDX analysis, the crystallites are considered to evolve from the grains shown in Fig. 4(a) as a result of annealing. It is proposed that this phase possess an A-site cation-deficient type of perovskite (A_xBO_3) structure where A is the larger element Sr, and B, the smaller element Fe in this case. This implies that elemental redistribution has occurred at the interface with the Sr-rich amorphous phase Sr-Fe-O-Si. Because the BO_3 array in the perovskite structure forms a stable network, the large A cations at 12 coordinated sites can be vacant either partially or completely.[32] Perovskite oxides that are A-site deficient are known to form when B = Ti, Nb,

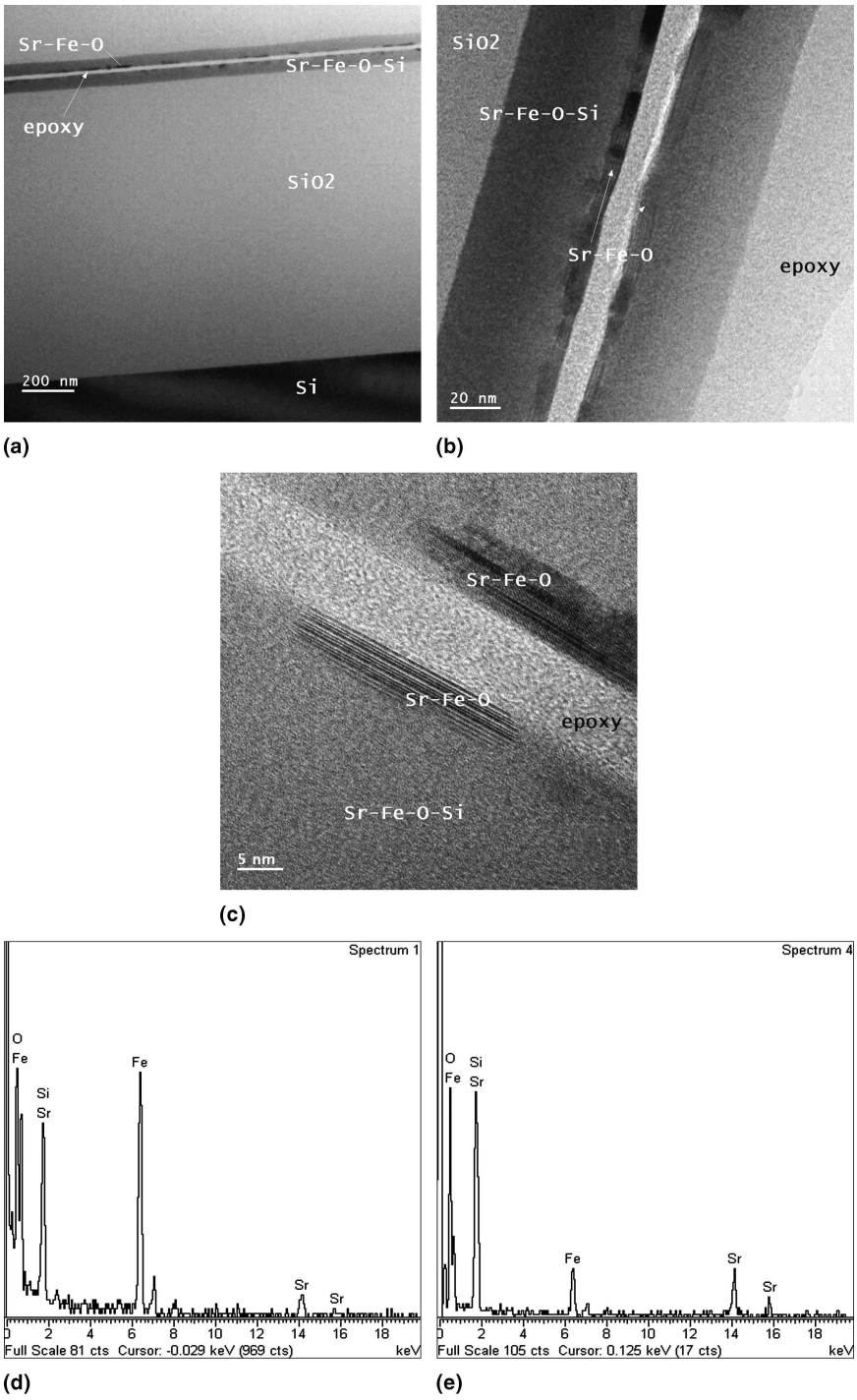

FIG. 6. TEM micrographs along with EDS spectra from a cross-section specimen of the $SrFeO_3/SiO_2/Si$ system deposited at 700 °C with an additional 1 h thermal annealing at $T = 700$ °C. (a) A BF TEM micrograph of a cross-section specimen showing the film/substrate structure. The film contains crystallites on top that are still labeled as Sr-Fe-O despite evidence that shows silicon is present and an amorphous phase labeled as Sr-Fe-O-Si. (b) An image with higher magnification from the area of the film. (c) A HRTEM image of a single crystallite in Sr-Fe-O. (d, e) EDS spectra from the Sr-Fe-O and Sr-Fe-O-Si layer, respectively.

Ta, etc.[33–37] Having examined the series of d-spacings converted from the diffraction pattern shown in Fig. 7(a), the phase that gives closest match is $SrFe_{12}O_{19}$ (PDF No. 46-0335). However, the *d*-spacing indicated by the diffraction pattern cannot uniquely identify the phase as a known Sr-Fe-O compound at this stage due to incomplete diffraction data because of preferred orientation effects. Therefore, a conclusive identification cannot be found by solely employing a *d*-spacing match with a known compound. A Fourier transform (analogy to

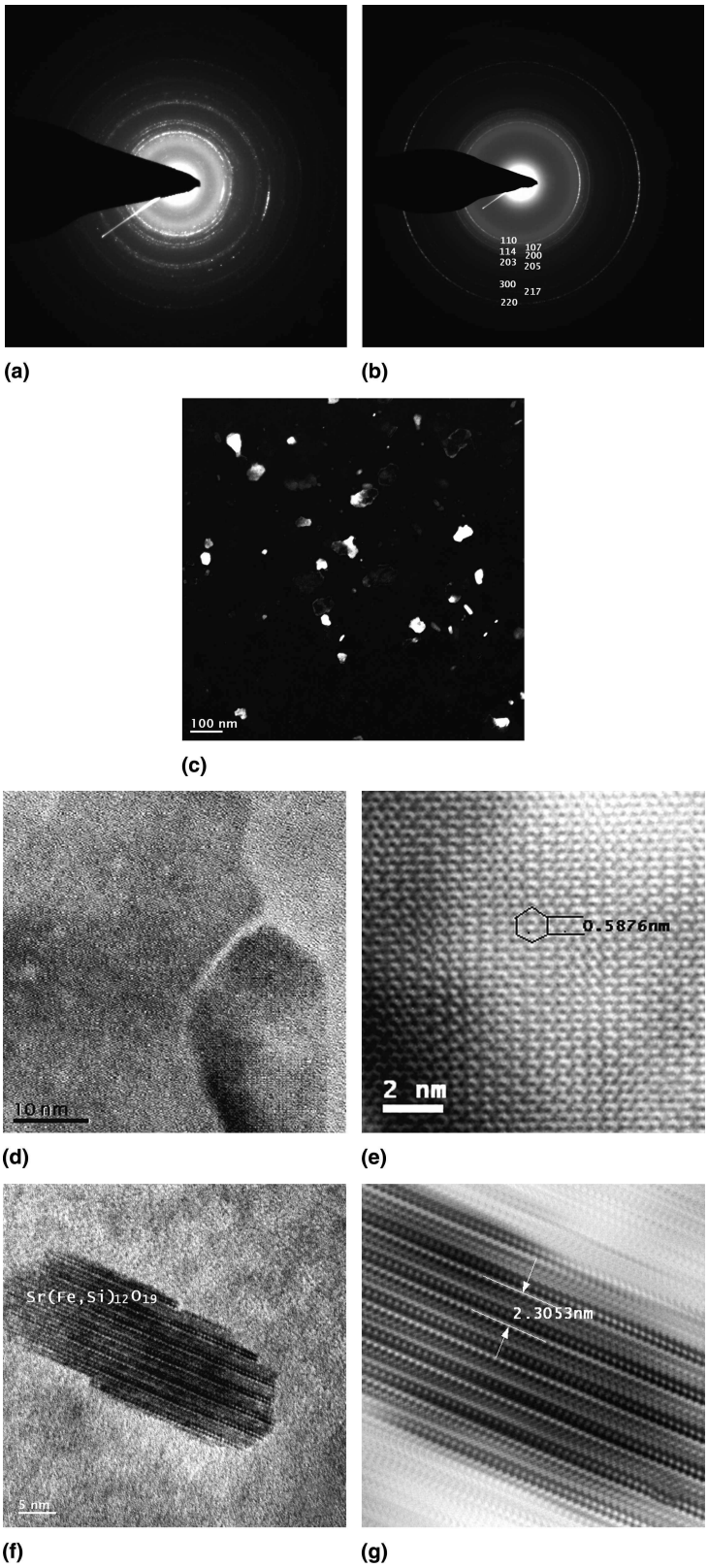

FIG. 7. ED patterns of the crystallites in the film deposited at 700 °C with (a) 1 h and (b) 3 h additional annealing at T = 700 °C. Differences are due to development of preferential orientation of the crystallites. (c) A DF image from the diffraction beam indicated by the index 110 in (b). (d) A HRTEM image of an individual crystallite from the plan view specimen shown in (c). (e) The filtered image aided by FFT of the crystallite shown in (d), which represents the lattice projection along c exhibiting hexagonal symmetry with $a = 0.5876$ nm. (f) A HRTEM image of a individual crystallite and its FFT filtered image (g) that represents the projection of the lattice along the direction parallel to the crystal plane shown in (e) with a periodicity of $c = 2.3053$ nm.

diffraction, not shown here) from a single crystal as shown in Fig. 6(c) yielded a lattice periodicity of 1.1545 nm in the direction perpendicular to the lamella layers of the crystallite structure implying a lattice parameter that could be equal to $n \times 1.1545$ nm (where n is an integer).

Definitive crystal structure identification of the outermost crystallites was achieved by combining HRTEM image analysis with electron diffraction obtained from the film system with longer-term annealing, at $T = 700$ °C for 3 h in this case. Crystal growth during this thermal treatment results in the evolution of preferential orientation as seen in Fig. 7(b) showing stronger texturing compared with that present in Fig. 7(a). Although the preferential orientation limits identification of the structure by electron diffraction due to an incomplete series of diffraction rings, it does facilitate crystallographic analysis using HR imaging. Thus, the crystal structure of the crystallites was revealed by HRTEM images obtained along its lattice direction. The c direction has been identified in the cross section as being perpendicular to the surface. The a and b cell parameters of the crystallites were subsequently determined by obtaining a DF TEM image [Fig. 7(c)] from the (110) diffraction beam indicated in Fig. 7(b) to confirm the corresponding relationship between the diffraction and the crystallites on the top surface of the film. HRTEM images from the crystallites were then obtained as shown in Fig. 7(d) along with its processed image aided by fast Fourier-transform (FFT) shown in Fig. 7(e) which represents the lattice projection along c exhibiting a hexagonal lattice with $a = 0.5876$ nm.

A HRTEM image and its FFT processed image shown in Figs. 7(f) and 7(g) represent the projection of the lattice along the direction parallel to the crystal plane shown in Fig. 7(e) exhibiting a periodicity of the lattice, $c = 2.3053$ nm, which is approximately equal to twice 1.1454 nm described previously as a possible lattice periodicity, suggesting that a sub-lattice structure exists and that the lattice parameter of the crystallites is $c = 2.3053$ nm. The result is a match to the phase $SrFe_{12}O_{19}$, which is hexagonal with parameters $a = 0.5887$ nm and $c = 2.3037$ nm. Therefore, this phase is isostructural with $SrFe_{12}O_{19}$. Considering that silicon is present in this phase, the overall structure is suggested as a type of intergrowth of perovskite ABO_3 and BO_3 with oxygen vacancies and Si partially replacing Fe, with a formula denoted as $Sr(Fe,Si)_{12}O_{19}$.

The mechanism of the evolution of the phase transformations in the $SrFeO_3/SiO_2/Si$ system has been developed from data presented by the images shown in Fig. 8. Figure 8(a) is an image indicating that the lamellar lattice structure of the crystallites extends through a transition zone into the amorphous phase surrounding it. Crystalline growth occurs gradually through a process of atomic rearrangement in the transition zone. Another type of atomic rearrangement has also occurred in the phase transformation, as indicated by an arrow in Fig. 8(b). This transformation appears to be due to the movement of atoms through the amorphous matrix phase toward the growing crystalline phase by way of filling the atomic

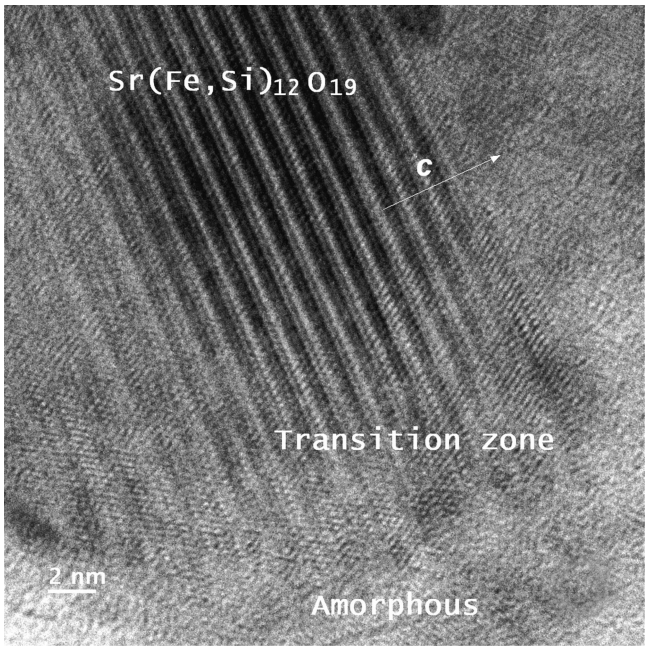

(a)

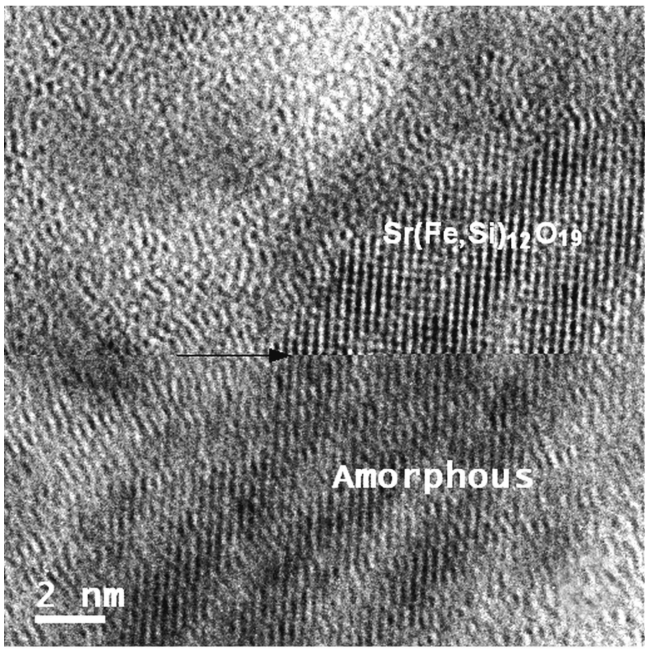

(b)

FIG. 8. HRTEM images from the $SrFeO_3/SiO_2/Si$ system deposited at 700 °C for 4 min and annealed for 1 h showing the growth of a crystallite into the amorphous surroundings by means of atomic rearrangement through the transition zone (a), and by adding atoms from the amorphous phase to the steps of a crystal plane indicated by the arrow (b).

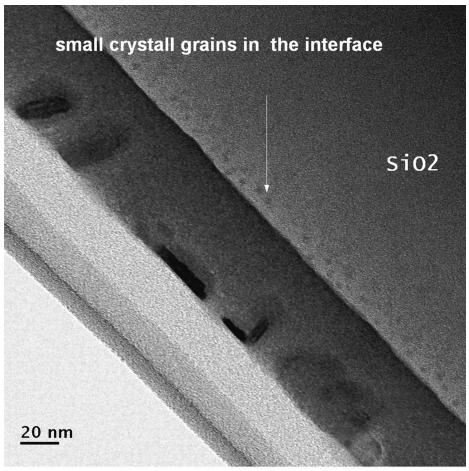

(a)

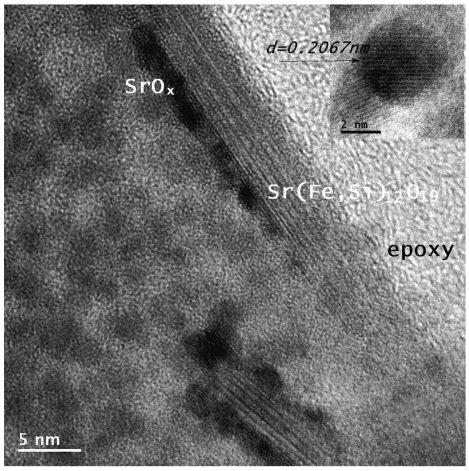

(b)

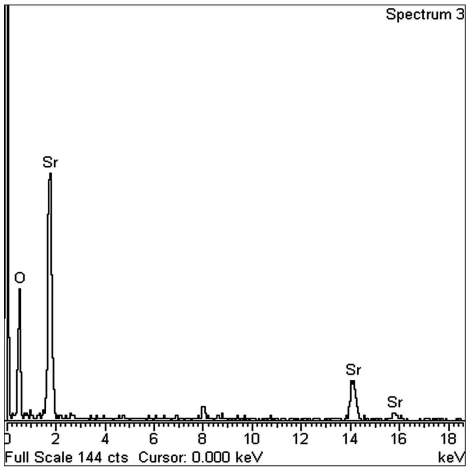

(c)

FIG. 9. (a) A cross-section image of the film system deposited at 700 °C with 3 h additional annealing at 700 °C. Larger, fewer, and less continuous crystallites are seen. A row of small grains appear in SiO_2 near the interface to the amorphous phase. (b) A HRTEM image along with an inset indicating that small crystal grains have precipitated from the amorphous matrix and appeared adjacent to the $Sr(Fe,Si)_{12}O_{19}$ phase. (c) EDS spectra from the crystalline grain adjacent to $Sr(Fe,Si)_{12}O_{19}$.

lattice steps at the interface. Thus, the new phase grows by consuming the amorphous matrix phase.

With increasing annealing time, the phase transformation and phase separation further develop in the films. Figure 9(a) shows a cross-section image of the film system deposited at 700 °C for 4 min and then annealed for 3 h. The crystallites no longer retain layer-like continuity at the outermost surface of the film and the number of the crystallites is reduced. This implies that crystal growth has occurred, with crystallites predominantly displaying two orientations; one parallel and one almost perpendicular to the surface of the film. Additionally, a row of nano-sized grains with unidentified structure appear in the SiO_2 layer near the boundary of the Sr-Fe-O-Si/SiO_2 interface shown in Fig. 9(a). Evidence for further phase separation is found, as shown in Fig. 9(b) where small crystal grains have precipitated from the amorphous matrix adjacent to the lamellar structure of the phase $Sr(Fe,Si)_{12}O_{19}$. A HRTEM image with lattice fringes shown in the inset of Fig. 9(b) indicates that the precipitates are crystalline and ~3 nm in diameter. The precipitates are shown to have a strontium oxide (SrO_X) composition by EDS analysis as shown in Fig. 9(c). The occurrence of these crystalline grains is an indication of initiation of crystallization in the amorphous phase.

C. Summary of the evolution of interfacial reactions

Based on the evidence discussed previously and the data shown in Table I obtained from the combined measurements (TEM, EDS, etc.) on the system, a model for the interfacial reactions of the thin film system induced by interdiffusion is shown in Fig. 10 and outlined below.

(1) Interfacial reactions of the thin film system deposited at room temperature

There is no interfacial reaction occurring at this stage. The interfacial structure is described as $SrFeO_{3(nanocrys)}$/$SrFeO_{3(amor)}$/$SiO_{2(amor)}$/$Si_{(crys)}$,

where the subscripts nanocrys, amor, and crys denote nanocrystallites, amorphous and crystalline forms, respectively.

TABLE I. Summary of the measurement of the film thickness under deposition and heat treatment conditions.

Deposition and heat treatment condition	Thickness of individual layer in the film system		
	In the $SrFeO_3$ film		
	Crystal (nm)	Amorphous (nm)	SiO_2 (μm) (amorphous)
RT[a] deposition for 4 min	31	15	1.14
700 °C deposition for 4 min	15	55	1.17
700 °C deposition +700 °C 1 h annl.	10	42	1.16
700 °C deposition +700 °C 3 h annl.	50		1.16

[a] RT, room temperature.

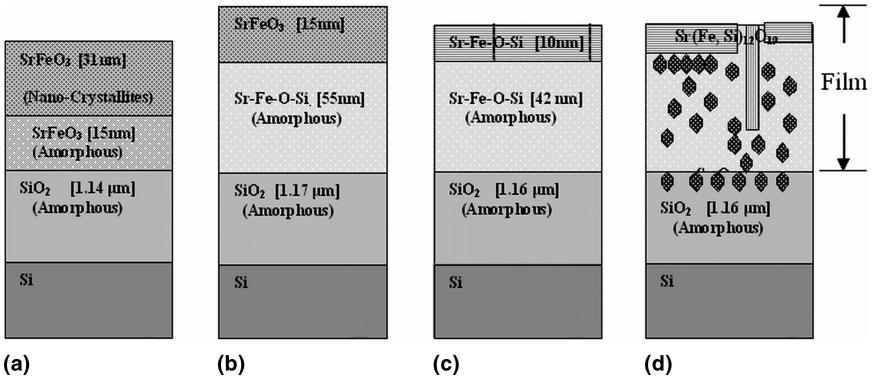

FIG. 10. Schematic illustrations of the changes in film thickness and interface structure at different deposition and thermal treatment conditions. (a) RT for 4 min as-deposited thin film system. (b) 700 °C for 4 min as-deposited thin film system. (c) Thin film system of 700 °C as-deposited with 1 h further thermal annealing at 700 °C. (d) Thin film system of 700 °C as-deposited with 3 h additional annealing at 700 °C.

(2) Interfacial reactions of the thin film system deposited at 700 °C

(a) In the as-deposited system, simultaneous film deposition and diffusion resulted in the reaction $SrFeO_{3(nanocrys)} + SiO_2 \rightarrow (Sr\text{-}Fe\text{-}O\text{-}Si)_{amor}$.

The interface structure is described as

$SrFeO_{3(nanocrys)}$ $[(SrFeO_3)_{[111]} + (SrFeO_3)_{[112]}]/(Sr\text{-}Fe\text{-}O\text{-}Si)_{amor}/SiO_2/Si$.

(b) In the system annealed for 1 h, elemental redistribution between

$SrFeO_{3(nanocrys)}$ and $(Sr\text{-}Fe\text{-}O\text{-}Si)_{amor}$ resulted in a phase transformation and separation forming an interface of $Sr(Fe,Si)_{12}O_{19}/(Sr_{(rich)}\text{-}Fe\text{-}O\text{-}Si)_{(amor)}$. The reaction is described as

$SrFeO_{3(nanocrys)} + (Sr\text{-}Fe\text{-}O\text{-}Si)_{amor} \rightarrow Sr(Fe,Si)_{12}O_{19} + (Sr_{(rich)}\text{-}Fe\text{-}O\text{-}Si)_{(amor)}$.

(c) Further annealing (2–10 h) resulted in the crystal growth of $Sr(Fe,Si)_{12}O_{19}$, formation of nano-sized SrO_X crystallites in the $(Sr_{(rich)}\text{-}Fe\text{-}O\text{-}Si)_{(amor)}$ amorphous phase and interdiffusion between SiO_2 and the film. The sum of the reactions are described as

$Sr(Fe,Si)_{12}O_{19(smaller\ crys.)} + (Sr_{(rich)}\text{-}Fe\text{-}O\text{-}Si)_{(amor)} + SiO_2 \rightarrow Sr(Fe,Si)_{12}O_{19\ (larger\ crys.)} + SrO_X$ + an unidentified phase (in the SiO_2 region).

IV. CONCLUSIONS

There were no interfacial reactions observed in the $SrFeO_3/SiO_2/Si$ system deposited at room temperature. The $SrFeO_3$ film was characterized as a layer of nano-sized crystal domains with a layer of an amorphous phase of the same elemental composition adjacent to the SiO_2/Si substrate. No preferential orientation occurs. When deposited at 700 °C for 4 min, the $SrFeO_3$ film of the $SrFeO_3/SiO_2/Si$ system exhibited a double phase (layered) structure. This included a layer of crystalline grains with preferential orientations [111] and [112] perpendicular to the surface, and a layered amorphous phase containing Sr, Fe, O with additional silicon. Following annealing at 700 °C for 1 h, the crystalline $SrFeO_3$ layer transformed to a hexagonal phase $Sr(Fe,Si)_{12}O_{19}$ with the lattice parameters *a* and *c* identical to the known compound $SrFe_{12}O_{19}$ but with additional Si, and leaving an amorphous layer comprising strontium, iron, and silicon adjacent to it. Longer period annealing resulted in an increased growth of the previously identified crystalline phase $Sr(Fe,Si)_{12}O_{19}$ and additional crystallization within the amorphous region of the film forming crystalline grains with composition identified as SrO_X. The existence of SiO_2, as a buffer layer on the silicon substrate, promoted the formation of amorphous phases in the film at the $SrFeO_3/SiO_2$ interface and was the source of thermal diffusion of silicon into the perovskite thin film. Consequently, SiO_2 is not a suitable choice of material for a diffusion barrier to construct stable $SrFeO_3$ thin film gas sensors for silicon-based MEMS structures, which require operation at elevated temperatures.

REFERENCES

1. K. Ichimura, Y. Inoue, and I. Yasumori: Hydrogenation and hydrogenalysis of hydrocarbons on perovskite oxides, in *Properties and Applications of Perovskite-Type Oxides,* edited by L.G. Tejuca and J.L.G. Fierro (Marcel Dekker, New York, 1993), p. 235.
2. B. Viswanathan: Co oxidation and NO reduction on perovskite oxides, in *Properties and Applications of Perovskite-Type Oxides,* edited by L.G. Tejuca and J.L.G. Fierro (Marcel Dekker, New York, 1993), p. 271.
3. T. Arakawa: Perovskite oxides as solid state chemical sensors, in *Properties and Applications of Perovskite-Type Oxides,* edited by L.G. Tejuca and J.L.G. Fierro (Marcel Dekker, New York, 1993), p. 361.
4. D.E. Williams: Conduction and gas response of semiconductor gas sensors, in *Solid State Gas Sensors,* edited by P.T. Moseley and B.C. Tofield (The Adam Hilger Series on Sensors, Bristol and Philadelphia, 1987), p. 71.
5. G. Eranna, B.C. Joshi, D.P. Runthala, and R.P. Gupta: Oxide

materials for development of integrated gas sensors—A comprehensive review. *Crit. Rev. Solid State Mater. Sci.* **29,** 111 (2004).
6. M.L. Post, J.J. Tunney, D. Yang, X. Du, and D.L. Singleton: Material chemistry of perovskite compounds as chemical sensors. *Sens. Actuators, B* **59,** 190 (1999).
7. J.J. Tunney, M.L. Post, X. Du, and D. Yang: Temperature dependence and gas-sensing response of conduction for mixed conducting $SrFe_yCo_zO_x$ thin films. *J. Electrochem. Soc.* **149**(6), H113 (2002).
8. G. Martinelli, M.C. Carotta, M. Ferroni, Y. Sadaoka, and E. Traversa: Screen printed perovskite-type thick films as gas sensors for environmental monitoring. *Sens. Actuators, B* **55,** 99 (1999).
9. J.P. Hodges, S. Short, J.D. Jorgensen, X. Xiong, B. Dabrowski, S.M. Mini, and C.W. Kimball: Evolution of oxygen-vacancy ordered crystal structures in the perovskite series $Sr_nFe_nO_{3n-1}$ (n = 2, 4, 8, and ∞), and the relationship to electronic and magnetic properties. *J. Solid State Chem.* **151,** 190 (2000).
10. Y. Takeda, K. Kanno, T. Takada, O. Yamamoto, M. Takano, N. Nakayama, and Y. Bando: Phase relation in the oxygen nonstoichiometric system, $SrFeO_x$ ($2.5 <= x <= 3.0$). *J. Solid State Chem.* **63,** 237 (1986).
11. M.L. Post, B.W. Sanders, and P. Kennepohl: Thin films of nonstoichiometric perovskites as potential oxygen sensors. *Sens. Actuators, B* **13–14,** 272 (1993).
12. J.J. Tunney and M.L. Post: The electrical conductance of $SrFeO_{2.5+x}$ thin films. *J. Electroceram.* **5**(1), 63 (2000).
13. K. Sahner, R. Moos, M. Matam, J.J. Tunney, and M.L. Post: Hydrocarbon sensing with thick and thin film p-type conducting perovskite materials. *Sens. Actuators, B* **108,** 102 (2005).
14. N. Barsan and U. Weimar: Conduction model of metal oxide gas sensors. *J. Electroceram.* **7,** 143 (2001).
15. C. Xu, J. Tamaki, N. Miura, and N. Yamazoe: Grain size effects on gas sensitivity of porous SnO_2-based elements. *Sens. Actuators, B* **3,** 147 (1991).
16. D.E. Williams and K.F.E. Pratt: Microstructure effects on the response of gas-sensitive resistors based on semiconducting oxides. *Sens. Actuators, B* **70,** 214 (2000).
17. Z. Wang, T. Sasaki, N. Koshizaki, J.J. Tunney, and M.L. Post: Crystallized $SeFeO_{3-x}$ films deposited by pulsed laser deposition without in-situ substrate heating. *Thin Solid Films* **437,** 95 (2003).
18. B.R. Sanders, J. Yao, and M.L. Post: Thin films of $SrFeO_{2.5+x}$—Effect of preferred orientation on oxygen uptake, in *Polycrystalline Thin Films: Structure, Texture, Properties and Applications,* edited by K. Barmak, M.A. Parker, J.A. Floro, R. Sinclair, and D.A. Smith (Mater. Res. Soc. Symp. Proc. **343,** Pittsburgh, PA, 1994), p. 463.
19. J.J. Tunney, P. Whitfield, X. Du, and M.L. Post: Pulsed laser deposition, characterization and thermochemical stability of $SrFe_yCo_{1-y}O_x$ thin films. *Thin Solid Films* **42,** 221 (2003).
20. R. Moos, F. Rettig, A. Hürland, and C. Plog: Temperature-independent resistive oxygen exhaust gas sensor for lean-burn engines in thick- film technology. *Sens. Actuators, B* **93,** 43 (2003).
21. S.J. Litzelman, A. Rothschild, and H.L. Tuller: The electrical properties and stability of $SrTi_{0.65}Fe_{0.35}O_{3-\delta}$ thin films for automotive oxygen sensor applications. *Sens. Actuators, B* **108,** 231 (2005).
22. X.F. Chen, H. Lu, W.G. Zhu, and O.K. Tan: Enhanced field emission of silicon tips coated with sol–gel-derived $(Ba_{0.65}Sr_{0.35})TiO_3$ thin film. *Surf. Coat. Technol.* **198,** 266 (2005).
23. S.H. Oh and C-G. Park: Nanoscale characterization of interfacial reactions in $SrRuO_3$ thin film on Si substrate. *Surf. Interface Anal.* **31,** 796 (2001).
24. X.B. Lu, X. Zhang, R. Huang, H.B. Lu, Z.H. Chen, W.F. Xiang, M. He, B.L. Cheng, H.W. Zhou, X.P. Wang, C.Z. Wang, and B.Y. Nguyen: Thermal stability of $LaAlO_3$/Si deposited by laser molecular-beam epitaxy. *Appl. Phys. Lett.* **84,** 2620 (2004).
25. X.B. Lu, Z.G. Liu, G.H. Shi, H.Q. Ling, H.W. Zhou, X.P. Wang, and B.Y. Nguyen: Interfacial structures of $LaAlO_3$ films on Si(100) substrates. *Appl. Phys. A. Mater. Sci. Process.* **78,** 921 (2004).
26. J.Q. He, C.L. Jia, V. Vaithyanathan, D.G. Schlom, J. Schubert, A. Gerber, H.H. Kohlstedt, and R.H. Wang: Interfacial reaction in the growth of epitaxial $SrTiO_3$ thin films on (001) Si substrates. *J. Appl. Phys.* **97,** 104921 (2005).
27. O. Grudin, R. Minescu, L.M. Landsberger, M. Kahrizi, G. Frolov, J.D.N. Cheeke, S. Chehab, M. Post, J. Tunney, X. Du, D. Yang, and D. Segall: High-temperature gas sensor using perovskite thin films on a suspended microheater. *J. Vac. Sci. Technol. A* **20**(3), 1100 (2002).
28. M. Ohring: *Material Science of Thin Films,* 2nd ed. (Academic Press, San Diego, 2002), p. 682.
29. D.K. Fork: Epitaxial oxides on semiconductors, in *Pulsed Laser Deposition of Thin Films,* edited by D.B. Chrisey and G.K. Hubler (John Wiley and Sons, Inc., New York, 1994), Chap. 16.
30. P.J. Goodhew: *Specimen Preparation for Transmission Electron Microscopy of Materials* (Oxford; New York: Oxford University Press; Oxford: Royal Microscopical Society, 1984).
31. D.G. Ivey and G.R. Piercy: Cross-sectional TEM specimens of metal contacts to semiconductors. *J. Electron Micr. Tech.* **8,** 233 (1988).
32. C.N.R. Rao, J. Gopalakrishnan, and K. Vidyasagar: Superstructures, ordered defects, and nonstoichiometry in metal oxides of perovskite and related structures. *Indian J. Chem.* **23A,** 265 (1984).
33. O.T. Sorensen: Thermodynamics and defect structure of nonstoichiometric oxides, in *Nonstoichiometric Oxides,* edited by O.T. Sorensen (Academic Press, New York, 1981), Chap. 1, p. 1.
34. LeRoy Eyring: Structure, defects, and nonstoichiometry in oxides: An electron microscopic view, in *Nonstoichiometric Oxides,* edited by O.T. Sorensen (Academic Press, New York, 1981), p. 338.
35. J.S. Anderson: The real structure of defect solids, in *Defects and Transport in Oxides,* edited by M.S. Seltzer and R.I. Jaffe (Plenum Press, New York, 1974), p. 25.
36. R.J.D. Tilley: Defect crystal chemistry and its applications, in *Chemical Physics of Solids and Their Surfaces,* Vol. 8, edited by M.W. Roberts and J.M. Thomas (Royal Society of Chemistry, London, 1980), p. 121.
37. C.N.R. Rao and G.V. Subba Rao: Electrical conduction in metal oxides. *Phys. Status Solidi.* **A1,** 597 (1970).